EDGE ARTICLE

Check for updates

Hierarchical tandem assembly of planar [3×3] building units into {3×[3×3]} oligomers: mixed-valency, electrical conductivity and magnetism†

Fei Yu, [ID] [a] Mohamedally Kurmoo, [ID] [b] Gui-Lin Zhuang [ID] [c] and Jing-Lin Zuo [ID] *[a]

A hierarchical tandem assembly – coordination, oligomerisation and supramolecular organization – is identified using MALDI-TOF of the solid products of the solvothermal reaction of 5,5′-pyridyl-3,3′-bi-1*H*-pyrazole with $CuSO_4 \cdot 5H_2O$ in CH_3OH–CH_3CN. The initial coordination leads to a [3×3] $[Cu_4^ICu_5^{II}(L)_6]$ $(SO_4) \cdot 2CH_3OH$ (**Cu₉**) grid followed by oligomerisation to a 3×[3×3] $[Cu_6^ICu_{21}^{II}(L)_{18}(CN)_6(SO_4)](SO_4)_2 \cdot 8CH_3CN$ (**Cu₂₇**) grid through bridging sulfate and *in situ* generated cyanide with time and subsequent supramolecular organization. The isolated silvery lustrous crystals, **Cu₉** and **Cu₂₇**, are good electrical conductors, with conductivities of 3.2×10^{-2} and 5.4×10^{-3} S cm^{-1}, respectively, due to the mixed valency. Their magnetic properties are dominated by antiferromagnetic interactions. DFT and band structure calculations confirm their valence distribution and semiconducting behavior. The planarity of the large 3×[3×3] **Cu₂₇** and its electro-activity renders it suitable for the development of large surface area molecular devices.

Introduction

Hierarchical assembly is involved in many processes.[1,2] These processes use recognition and supramolecular matching of chemical pairs to help with the organization.[3–5] In chemistry the acquired knowledge from biology is used in the design of organic dendrimers, polymers and molecular machines and extended to coordination compounds as well as metal–organic frameworks.[6–10] In physics the modelling of nanostructures on surfaces is a major active area of development as is patterning for logic circuits.[11] Although hierarchical assembly processes have been recognized in chemistry, tandem ones are rarely evoked.[12,13]

In the course of studying the coordination complexes obtained from different copper salts with planar multidentate 5,5′-pyridyl-3,3′-bi-1*H*-pyrazole, rich in π-electrons, by solvothermal reactions in different solvents, we have isolated several series of complexes of variable nuclearities and valencies. One series contains rugby-ball hexamers where the valence of the copper ions varies from Cu_6^{II} to $Cu^ICu_5^{II}$ and $Cu_2^ICu_4^{II}$ depending on the

anions.[14] While the former monovalent compound is an insulator, those with mixed Cu^I/Cu^{II} are semiconductors. Other crystalline variants were obtained by tuning the solvents and the time of the solvothermal treatment. Using MALDI-TOF of the solids at different periods of the reaction, we have identified a hierarchical tandem assembly starting from the coordination of the ingredients to form [3×3] $[Cu_4^ICu_5^{II}(L)_6](SO_4) \cdot 2CH_3OH$ (**Cu₉**) followed by its oligomerisation to a giant 3×[3×3] $[Cu_6^ICu_{21}^{II}(L)_{18}(\mu_2\text{-CN})_6(\mu_3\text{-SO}_4)](SO_4)_2 \cdot 8CH_3CN$ (**Cu₂₇**) disk and finally its supramolecular arrangement into a crystalline solid (Fig. 1). The two solids **Cu₉** and **Cu₂₇** were isolated from pure methanol and a mixture of methanol and acetonitrile, respectively.

Herein, we report their crystal structures (Tables 1, S1, and S2†) and characterization using powder diffraction (Fig. S1†), infrared and photoelectron spectroscopies and
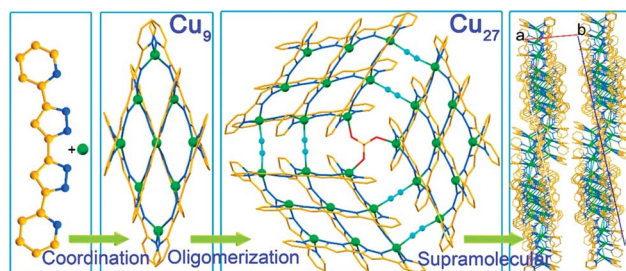
[a] State Key Laboratory of Coordination Chemistry, School of Chemistry and Chemical Engineering, Collaborative Innovation Center of Advanced Microstructures, Nanjing University, Nanjing, 210023, P. R. China. E-mail: zuojl@nju.edu.cn

[b] Institut de Chimie de Strasbourg, Université de Strasbourg, CNRS-UMR 7177, 4 rue Blaise Pascal, 67008 Strasbourg, France

[c] College of Chemical Engineering, Zhejiang University of Technology, Hangzhou, 310032, P. R. China

† Electronic supplementary information (ESI) available. CCDC 1844367 and 1844368. For ESI and crystallographic data in CIF or other electronic format see DOI: 10.1039/c8sc02851f

Fig. 1 The three-step tandem hierarchy in obtaining **Cu₂₇** from Cu (green), 5,5′-pyridyl-3,3′-bi-1*H*-pyrazole (rust and blue) and sulphate (red and yellow) and cyanide (cyan) bridges *via* **Cu₉**.

thermogravimetry (Fig. S2†) together with an experimental study of their electrical, magnetic and optical properties. DFT and band structure calculations were performed to understand the valence distribution and the unusual electrical conductivity. Considerable differences in the electrical and magnetic properties were observed which depend on the average oxidation state of the copper ions. The results are quite exceptional for this series of materials where the central metal moieties provide variable carriers, where their electronic densities and magnetic moments increase with the number of metals and their valences, while the organic ligands interact with those of neighbouring units creating bands favouring electron-transfer.[13] This particular distribution of charges and spins is quite unique in rendering these solids electrically conducting.

Results and discussion

Synthesis

The planar multidentate pyridine–pyrazole ligand H_2L was synthesized by slight modification of a previously reported procedure.[14–16] Solvothermal reaction of the ligand, neutralized with triethylamine, with cupric sulphate in methanol leads to silvery hexagonal crystals of the nonanuclear $[Cu_4^ICu_5^{II}(L)_6]$-$(SO_4)\cdot 2CH_3OH$ (Cu_9), whereas that in a mixture of methanol and acetonitrile leads to silvery square blocks of the heptacosanuclear $[Cu_6^ICu_{21}^{II}(L)_{18}(\mu_2\text{-}CN)_6(\mu_3\text{-}SO_4)](SO_4)_2\cdot 8CH_3CN$ (Cu_{27}).

Crystal structures

The structure of Cu_9 has a planar nonanuclear $[3\times3]$ grid core of copper atoms enveloped by six organic ligands, three above the metal plane and three below. The ligands are almost perpendicular to the metal plane and three on one face are parallel to each other but the other three are almost orthogonal to those on the opposite face. There are slight differences in ligand and metal coordination depending on the positions of the copper atoms and their valences while the crystal symmetry of the cluster is satisfied. The grid is highly deviated from a square in order to accommodate the chelating distances of the coordinating nitrogen pairs and the flattened tetrahedron of Cu^{II}. Cu_9 crystallizes in the monoclinic $C2/c$ space group and the molecular unit includes nine Cu atoms ($Cu_4^ICu_5^{II}$), six L^{2-} ligands, one SO_4^{2-} anion and two free methanol molecules. The nine metal ions can be categorized into three types: the four corner ones (Cu5, Cu5′, Cu4 and Cu6) each have four nitrogen atoms from two pyridines and two pyrazoles, while the four in the middle of the edges (Cu1, Cu3, Cu3′, and Cu1′) have four nitrogen atoms from one pyridine and three pyrazoles, and the central one (Cu2) has four nitrogen atoms from four pyrazoles (Fig. 1). All the copper ions have a $[CuN_4]$ coordination sphere and are connected by $N\cdots N$ bridges. The average Cu–N bond lengths are $[Cu1–N] = [Cu2–N] = [Cu3–N] = 1.96$, $[Cu4–N] = [Cu6–N] = 1.99$ and $[Cu5–N] = 2.02$ Å. They indicate that Cu4, Cu5, Cu5′ and Cu6 are Cu(I), while Cu1, Cu2, Cu3, Cu1′ and Cu3′ are Cu(II).

The ligands on each face stand in an offset parallel arrangement. The intramolecular $\pi\cdots\pi$ distances are rather short (3.3–3.5 Å) (Fig. S3†), indicating the presence of strong $\pi\cdots\pi$ interactions. The ligands between adjacent molecules are stacked through offset $\pi\cdots\pi$ bond-over-ring mode. The molecules form staircase-like one-dimensional (1D) arrays running along the b-axis with a face-to-face distance of 3.32 Å, suggesting strong interaction. Intermolecular H-bonds (Table S2†) between the 1D-arrays extend them into 2D layers in the ac-plane (Fig. S4 and S5 and Table S3†).

Cu_{27} is an oligomer of three Cu_9 with a $3\times[3\times3]$ heptacosanuclear structure with a distorted grid core of copper atoms enveloped by eighteen organic ligands and combined with one sulphate and six cyanide bridges. It has a pseudo-trigonal symmetry of three Cu_9 held together by a SO_4 sitting centrally on the C_3-axis and six bridging cyanide ions between the edges (Fig. S3†). The twenty-seven metal ions can be categorized into four types: the three corner ones (Cu9, Cu18, and Cu27) have four nitrogen atoms from two pyridines and two pyrazoles, and the average Cu–N bond lengths are $[Cu9–N] = 2.03$, $[Cu18–N] = 2.01$, and $[Cu27–N] = 2.04$ Å. The angles are $\angle N18–Cu9–N36 = 120.2°$ ($\angle N54–Cu18–N72 = 128.6°$, $\angle N90–Cu27–N108 = 122.7°$) and $\angle N17–Cu9–N35 = 157.0°$ ($\angle N53–Cu18–N71 = 161.4°$, $\angle N89–Cu27–N107 = 157.3°$). Their geometries are closer to a tetrahedron; thus, they are assigned to cuprous ions. The six atoms (Cu6, Cu15, Cu24, Cu8, Cu17, and Cu26) in the middle of the edges are four-coordinated ones with one pyridine and three pyrazoles and the average Cu–N bond lengths are $[Cu6–N] = [Cu24–N] = [Cu8–N] = [Cu17–N] = [Cu26–N] = 1.97$ and $[Cu15–N] = 1.95$ Å. The angles are $\angle N12–Cu6–N34 = 132.37°$ ($\angle N47–Cu15–N69 = 128.1°$, $\angle N84–Cu24–N106 = 129.5°$), $\angle N11–Cu6–N33 = 170.5°$ ($\angle N48–Cu15–N70 = 170.7°$, $\angle N84–Cu24–N106 = 170.3°$), $\angle N16–Cu8–N30 = 130.6°$ ($\angle N52–Cu17–N66 = 132.7°$, $\angle N88–Cu26–N102 = 135.1°$), and $\angle N15–Cu8–N29 = 170.5°$ ($\angle N51–Cu17–N65 = 170.3°$, $\angle N87–Cu26–N101 = 169.0°$). Their geometries are more planar; thus, they are assigned to cupric ions. The central ones (Cu5, Cu14, and Cu23) have four nitrogen atoms from four pyrazoles. The average Cu–N bond lengths are $[Cu5–N] = 2.03$, $[Cu14–N] = 2.01$, and $[Cu23–N] = 2.04$ Å. The angles are $\angle N18–Cu9–N36 = 120.2°$ ($\angle N54–Cu18–N72 = 128.6°$, $\angle N90–Cu27–N108 = 122.7°$) and $\angle N17–Cu9–N35 = 157.0°$ ($\angle N53–Cu18–N71 = 161.4°$, $\angle N89–Cu27–N107 = 157.3°$). Their geometries are close to a tetrahedron, and thus they are assigned to cuprous ions (Fig. 1).

The intramolecular $\pi\cdots\pi$ distances remain short in the range 3.3–3.4 Å and C–H$\cdots\pi$ distances of 2.60–2.89 Å are short and lie in the bc-plane. The adjacent molecules are stacked through the strong, offset $\pi\cdots\pi$ interaction with a face-to-face distance of 3.35 Å to furnish staircase-like one-dimensional (1D) arrays running along the b-axis (Fig. S4†). Intermolecular C–H$\cdots\pi$ between the 1D-arrays extend them into 2D layers in the bc-plane (Fig. S5 and S6 and Table S3†). These 2D layers form 3D supramolecular frameworks by using acetonitrile molecules and sulphate anions.

MALDI-TOF

While Cu_9 was isolated as crystals in pure methanol, the presence of acetonitrile was found to be indispensable for the crystallization of Cu_{27}. It was therefore necessary to understand

the relation between the two compounds. We therefore studied the MALDI-TOF MS of the solids formed from a mixture of methanol and acetonitrile as a function of time (Fig. 2).

For the solids, by 30 minutes only peaks assignable to **Cu$_9$** were located for the black product. Their intensities increase up to 2 hours when the peaks for **Cu$_{27}$** start to appear. The quantity of the **Cu$_{27}$** then increases at the expense of **Cu$_9$** with time. Even after 24 hours there is still a trace of **Cu$_9$** but the bulk comprises crystals suitable for crystallography. It is therefore clear from a mechanistic point of view that the initial step is the coordination of the ligand to give the [3×3] **Cu$_9$** grid cluster and with time the **Cu$_9$** units are oligomerized to the 3×[3×3] **Cu$_{27}$** cluster with the help of bridging SO_4 and *in situ* generated cyanide ions. The final step is the crystallization using the supramolecular interactions. It is worth noting that crystals of **Cu$_{27}$** are insoluble in organic solvents compared to those of **Cu$_9$**. Interestingly, **Cu$_9$** is obtained starting from different copper salts and different solvents but **Cu$_{27}$** is obtained only in the presence of SO_4 and acetonitrile. The three step hierarchical process is new in the chemistry of oligomerisation of clusters.

X-ray photoelectron spectroscopy and spin density calculations

The valence states of the copper ions and their proportions in the compounds were determined from X-ray photoelectron spectroscopy. The $2p_{1/2}$ and $2p_{3/2}$ peaks are characterized by doublets for both **Cu$_9$** and **Cu$_{27}$**. The energies of the $2p_{3/2}$ doublet are 934.8 and 931.9 eV (Fig. 3), corresponding to Cu^{II} and Cu^{I}, respectively.[17] A similar observation was made for the $2p_{1/2}$ peaks. Analysis of the areas of these two peaks gave $Cu^{I} : Cu^{II}$ ratios of 43 : 57 and 23 : 77 respectively, consistent with the calculated balance of charge of the formula and crystallographic findings of $4Cu^{I} : 5Cu^{II}$ and $2Cu^{I} : 7Cu^{II}$ for **Cu$_9$** and **Cu$_{27}$**. It is noted that the complete structural characterization from single crystals of the

Fig. 3 Cu-$2p_{3/2}$ valence band XPS spectra of (a) **Cu$_9$** and (b) **Cu$_{27}$**. Spin density distributions (green is positive and blue is negative) for (c) **Cu$_9$** and (d) **Cu$_{27}$**. The black labels are for Cu(ɪɪ) and the pink labels are for Cu(ɪ).

mixed valence of a common molecular brick is quite rare. The presence of different valences is very interesting in view of charge delocalization and thus band-filling. They are consequently reflected in the conductivity, which is also important in magnetic properties because of the similar structure with different numbers of spin carriers. In contrast to crystallographic data, XPS gives a more accurate definition of the valence states of the compounds and confirms that they belong to Class II of the mixed-valence classification.[18]

Spin density calculations were performed for the two compounds built from the experimentally determined geometries with H atom optimization (Fig. 3 and Table S4†).[19] We find that they are centred principally on the Cu atoms with some delocalization on the coordinated nitrogen atoms. Very little spin density is diffused onto the carbon atoms of the organic ligands. The oxidation states were evaluated by the localized orbital bonding analysis (LOBA) method within Mutliwfn and the results are presented in Table S4.†[20] The results indicated that Cu4, Cu5, Cu5′ and Cu6 are Cu(ɪ), and the remaining copper ions are Cu(ɪɪ) in **Cu$_9$** and Cu5, Cu9, Cu14, Cu18, Cu23 and Cu27 are Cu(ɪ), while all the other copper ions are Cu(ɪɪ) in **Cu$_{27}$**.

Electrical conductivity

The high absorption and silvery lustre of the crystals are consistent with the mixed-valence found and therefore, they are

Fig. 2 MALDI-TOF mass spectra of the solid products as a function of time of solvothermal treatment.

expected to be conducting (Fig. S7†). Gold wires were attached on the surface using silver paste for two-probe resistance and $I-V$ measurements at different temperatures. Measurements on single crystals of **Cu₉** found a room temperature conductivity of 3.2×10^{-2} S cm^{-1} along the *ab*-plane (almost parallel to the plane of the molecules) and 4.3×10^{-8} S cm^{-1} perpendicular to it. The temperature dependence of the resistivity in the *ab*-plane follows an Arrhenius behaviour with a fairly low activation energy of 0.02 eV. Measurements for single crystals of **Cu₂₇** found a slightly lower room temperature conductivity of 10^{-3} S cm^{-1} along the *bc*-plane of the molecules but a higher one of 10^{-5} S cm^{-1} perpendicular to it (Fig. 4). The crystals of **Cu₂₇** lose the solvents with time and the temperature dependence measurement was hampered due to the vacuum needed for the cryostat. Monitoring the crystals under an optical microscope during the solvent evaporation reveals a limited stability and appearance of cleavages after dryness, presumably between the layers (Fig. S8†). The observed values of conductivity are quite promising for such molecules where charge becomes mobile within the solid through supramolecular $\pi\cdots\pi$ interactions as is the low activation energy in the case of **Cu₉**.

Magnetic properties and electron paramagnetic resonance

The temperature dependences of the magnetic moments, represented by the product of susceptibility and temperature, for the two compounds are shown in Fig. 5. We caution that loss of solvent for **Cu₂₇** may have taken place but the molecular structure and valence state are not altered. The values of $\chi_M T$ at 300 K for the polycrystalline samples are 1.88 and 6.94 cm^3 mol^{-1} K for **Cu₉** and **Cu₂₇**, respectively. Curie–Weiss fits for data above 150 K gave respectively $C = 2.26$ and 9.53 cm^3 mol^{-1} K and $\theta = -70$ and -110 K. From the Curie constants the average g-value is 2.19 $\pm$ 0.01, which is reasonable for Cu^{2+}. The EPR spectra of polycrystalline samples are characterized by broad resonances ($\Delta H_{pp} = 172$ G and $g = 2.06$ (**Cu₉**) and 580 G

Fig. 5 The temperature dependence of $\chi_M T$ for **Cu₉** (red circles) and **Cu₂₇** (blue circles), measured in a field of 1.0 kOe. The solid black lines are the best fits (see text).

and $g = 2.10$ (**Cu₂₇**)) (Fig. S9†). The large negative Weiss constants indicate strong antiferromagnetic coupling between the nearest neighbouring Cu(ii) ions. The temperature dependences of the susceptibility were modelled using the Hamiltonian given in equations (ESI†) giving, for **Cu₉**, $g = 2.15$, $J_1 = -28.3$ cm^{-1} and $J_2 = -27.8$ cm^{-1}.[21] For **Cu₂₇**, due to the large number of Cu(ii) and the limitation of computer ability, it is impossible to apply the irreducible tensor operator method used in PHI. By modifying the LOOP code[22] of the Algorithms and Libraries for Physical Simulations (ALPS) project,[23] we herein coupled the Genetic Algorithm with the Quantum Monte Carlo (GA-QMC) method to search for the global optimal parameters.[24] Essentially, the entire spin exchange network per cluster (Fig. 5) was simplified to a 3 J model (see the Hamiltonian operator in the ESI†). In view of the large number of atoms per cluster and the considerable $\pi\cdots\pi$ supramolecular interaction, a temperature-independent paramagnetism (TIP) parameter and intercluster interaction (zJ) were respectively considered. After 200 iterations, the simulation yielded one set of optimal parameters: $J_1 = -4.9$ cm^{-1}, $J_2 = -210.7$ cm^{-1}, $J_3 = -3.8$ cm^{-1}, $g = 2.19$, TIP = 0.00 cm^3 mol^{-1}, $zJ = 0.01$ cm^{-1}, and $R = 4.25 \times 10^{-5}$ ($R = \sum[(\chi_M T)_{obs} - (\chi_M T)_{calcd}]^2 / \sum[(\chi_M T)_{obs}]^2$). The values of the moments are direct electron counts and give support to the XPS and crystallography results while the excellent fits suggest that a localized moment picture is an adequate representation. Interestingly, the exchange through the C≡N bridge is the strongest compared to those through the N=N bridge. The reduction in the values of the exchange interactions within the **Cu₉** segments of **Cu₂₇** may be due to the effect of the strong field of the bridging cyanide groups.

Optical properties

The optical properties of the compounds in the limiting region of 200–2000 nm were studied by diffuse reflectance
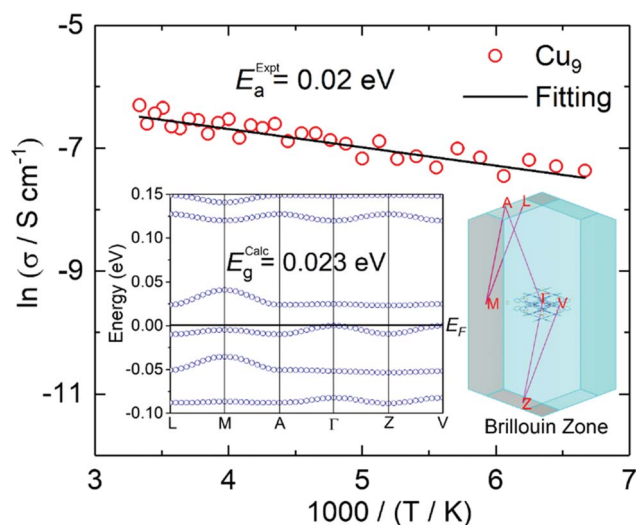

Fig. 4 Arrhenius plot of ln(resistance) *versus* scaled inverse temperature (red circles represent experimental data and the black line is the linear fit). Inset: calculated band structure and Brillouin zone.

Table 1 Crystallographic data and structure refinement details for Cu_9 and Cu_{27}

	Cu_9	Cu_{27}
Formula	$C_{98}H_{68}Cu_9N_{36}O_6S$	$C_{310}H_{204}Cu_{27}N_{122}O_{12}S_3$
Fw	2449.80	7641.69
Space group	$C2/c$	$P2_1/n$
a/Å	32.700(18)	14.7327(3)
b/Å	10.890(6)	47.3434(8)
c/Å	30.813(17)	51.2702(8)
β/°	114.970(7)	97.581(2)
V/Å^3	9947(9)	35 448.2(11)
Z	4	4
D_c/g cm^{-3}	1.630	1.432
T/K	150(2)	150(2)
$F(000)$	4900	14 292
R_{int}	0.059	0.065
$R_1{}^a$ [$I \geq 2\sigma(I)$]	0.070	0.066
$wR_2{}^b$ (all data)	0.214	0.141
GoF	1.00	1.02

^{a} $R_1 = \Sigma||F_o| - |F_c||/\Sigma|F_o|$. ^{b} $wR_2 = [\Sigma w(F_o{}^2 - F_c{}^2)^2/\Sigma w(F_o{}^2)^2]^{1/2}$.

measurements on the powdered samples in $BaSO_4$. The spectra, shown in Fig. S10,† present an edge in each case where a linear extrapolation was used to estimate the band gap. Surprisingly, considering the crude approximated extrapolation, there is a general trend in the spectra. The band-gaps were 0.03 and 0.25 eV for Cu_9 and Cu_{27}, respectively, which are close to those found by conductivity measurements and band structure calculations.

Conclusions

A hierarchical tandem assembly, including coordination to nonanuclear [3×3] Cu_9, its oligomerisation to a giant 3×[3×3] Cu_{27} cluster and finally the supramolecular organization into crystals, is achieved. The second step was revealed by MALDI-TOF and confirmed by single crystal diffraction. The oligomerisation step is facilitated by the presence of sulphate and *in situ* generated cyanide from acetonitrile. The oligomerisation is not observed in their absence. Their mixed-valence states were confirmed by X-ray photoelectron spectroscopy and the metallic lustre of the crystals is compatible with the fairly high electrical conductivities with three orders of magnitude anisotropy. The structure–electrical property relationship suggests that the $\pi\cdots\pi$ interaction between neighbouring molecules is the ingredient for the electron-transfer resulting in high conductivity and low activation energy. However, the magnetic susceptibility fittings to localized moment models are a clear indication that these two compounds belong to Class II of the mixed-valence classification. Furthermore, the experimental results are in good agreement with those estimated from DFT and band-structure calculations. Such large planar electroactive clusters which are highly absorbing in the visible region should be suitable for large surface area devices for harvesting light for energy purposes.

Experimental

Materials

All chemicals and solvents were obtained from commercial sources and utilized without further purification.

$[Cu_4^ICu_5^{II}(L)_6](SO_4)\cdot 2CH_3OH$ (Cu_9). A CH_3OH (8 mL, AR-grade $\geq$ 99.7%) solution of $CuSO_4\cdot 5H_2O$ (28.0 mg, 0.112 mmol) and H_2L (21.5 mg, 0.075 mmol) was adjusted to pH $\approx$ 8 with Et_3N in a 15 mL Pyrex vial which was then tightly capped and heated at 140 °C for 24 h. After the autoclave was cooled to 30 °C at a rate of 5 °C h^{-1}, the black needle shaped crystals of Cu_9 were collected within one hour, washed with methanol, and dried in air (yield: 15.2 mg, 46% based on the ligand). ESI-MS (positive mode, CH_3OH): m/z: 1144.97 $(C_{96}H_{60}N_{36}Cu_9)^{2+}$. Elemental analysis (%) calculated for $C_{98}H_{68}N_{36}O_6SCu_9$: C, 48.05; H, 2.80; N, 20.58; found: C, 48.56; H, 2.98; N, 20.22. Infrared (KBr, cm^{-1}): 3412(m), 3098(m), 1616(s), 1588(w), 1532(m), 1456(s), 1324(m), 1166(s), 1128(s), 1052(m), 986(m), 788(s), 612(m).

$[Cu_6^ICu_{21}^{II}(L)_{18}(CN)_6(SO_4)](SO_4)_2\cdot 8CH_3CN$ (Cu_{27}). A suspension of $CuSO_4\cdot 5H_2O$ (28.0 mg, 0.112 mmol) and H_2L (21.5 mg, 0.075 mmol) in a mixture of 4 mL CH_3OH and 4 mL CH_3CN was adjusted to pH $\approx$ 8 with Et_3N, filtered, and divided into two equal parts. The first part was slowly concentrated in air to give a black powder of a Cu_9 complex which was only identified by ESI-MS. The second part was placed in a 15 mL Pyrex vial which was tightly capped and heated at 140 °C for 24 h. After the autoclave was cooled at a rate of 5 °C h^{-1} to 30 °C, black square block shaped crystals of Cu_{27} were collected, washed with ethanol, and dried in air (yield: 32.0 mg, 53% based on the ligand). MALDI-TOF (positive mode): m/z: 7313.25 $\{[Cu_6^ICu_{21}^{II}(L)_{18}(CN)_6(SO_4)](SO_4)_2\}^+$. Elemental analysis (%) calculated for $C_{310}H_{204}Cu_{27}N_{122}O_{12}S_3$: C, 48.72; H, 2.69; N, 22.36; found: C, 48.53; H, 2.51; N, 22.65. Infrared (KBr, cm^{-1}): 2174(w), 2104(w), 1604(s), 1562(m), 1524(w), 1450(s), 1436(s), 1348(s), 1242(w), 1154(m), 1108(w), 1048(m), 988(m), 774(s), 714(m).

Measurements

The C, H and N microanalyses were carried out with a Vario Micro Cube elemental analyzer. Thermogravimetric analyses (TGA) were performed on a NETZSCH STA 449 F3 Jupiter TGA instrument in flowing N_2 at a heating rate of 5 °C per minute in the range of 40 to 800 °C. Samples for infrared (IR) were prepared as KBr pellets, and spectra were recorded in the 400–4000 cm^{-1} range using a Vector 22 Bruker spectrophotometer. UV-Vis-NIR spectra were recorded in diffuse reflectance mode on a UV-3600 Shimadzu spectrometer. Powder X-ray diffraction (PXRD) patterns were recorded at 293 K on a D8 ADVANCE (Cu Kα1, λ = 1.54056 Å; Kα2, λ = 1.54439 Å) powered at 40 kV and 40 mA. The powder samples were prepared by crushing the crystals and the PXRD scanned from 5 to 50° at a rate of 5° min^{-1}. Calculated PXRD patterns were generated using Mercury 3.9.[25] Mass spectra were recorded with an LCQ Fleet instrument for ESI-MS and an ultrafleXtreme TOF/TOF for MALDI-TOF/TOF mass spectrometry. Electron paramagnetic

resonance (EPR) spectra were recorded on a Bruker ER-420 spectrometer with a 100 kHz magnetic field in the X band at room temperature (RT). X-ray photoelectron spectroscopy (XPS) studies were performed using a Thermo Fisher ESCALAB 250 X-ray photoelectron spectrometer (powered at 150 W) using Al Kα radiation ($\lambda = 8.357$ Å). Magnetisation measurements for polycrystalline samples were performed on a Quantum Design MPMS-SQUID-VSM magnetometer in the temperature range from 1.8 to 300 K for direct current (dc) applied fields ranging from 0 to 70 kOe. Diamagnetic corrections were calculated using Pascal's constants,[26] and an experimental correction for the diamagnetic sample holder was applied. Temperature-dependent electrical conductivities and I–V curves were measured using a Keithley 4200 semiconductor parameter analyser using single crystal samples by the two-probe method using silver paste and gold wire contacts.

X-ray structure determination

The single-crystal X-ray diffraction data for **Cu₉** and **Cu₂₇** were collected on a Bruker D8 VENTURE diffractometer with a PHOTON 100 CMOS detector equipped with a Mo-target X-ray tube ($\lambda = 0.71073$ Å) at $T = 150$ K by using the φ–ω scan technique. Data were corrected for absorption using the empirical method SADABS.[27] The structures were solved using SHELXT[28] and refined using the full-matrix least-squares procedures within the SHELXTL software package.[29] All non-hydrogen atoms were refined with anisotropic displacement parameters. The hydrogen atoms were generated geometrically (C–H = 0.95 Å) using the riding model. For all structures, the guest molecules were further confirmed by thermogravimetric analyses (TGA). It was not possible to resolve diffuse electron density residuals (enclosed solvent molecules). The co-crystallized solvent molecules were squeezed with the SQUEEZE facility from PLATON:[30] 8CH₃CN for **Cu₂₇** (per asymmetric unit). Crystallographic information for all the complexes is presented in Table 1. Selected bond distances and angles are given in the ESI.† The crystallographic information files have been deposited at The Cambridge Crystallographic Data Centre with references 1844367 (**Cu₉**) and 1844368 (**Cu₂₇**); they can be obtained from http//:www.ccdc.cam.ac.uk/data_request/cif.

DFT calculations

All theoretical calculations were carried out at the DFT level of theory using the hybrid B3LYP/6-31g* exchange–correlation functional[31–33] as implemented in the Gaussian 09 program.[34] A quadratic convergence method was employed in the SCF process.[35] The triple-ζ quality basis set proposed by Ahlrichs and coworkers has been used for all atoms.[36] Calculations were performed on the complexes built from the experimentally determined geometries with H atom optimization.

Band structure calculations

To gain a good insight into the electrical and optical properties, we performed first-principles electronic structure calculations for **Cu₉** based on density functional theory with generalized gradient approximation (GGA) in the form of the Perdew–Burke–Ernzerhof (PBE) functional for exchange–correlation potential.[37] We used the Cambridge Serial Total Energy Package (CASTEP),[38] which is a self-consistent-field method (tolerance 5.0×10^{-5} eV per atom) in conjunction with plane-wave basis sets with a cut-off energy of 517 eV using OTFG ultrasoft pseudopotentials in reciprocal space.[39] Calculations were performed starting with the crystal structure data of **Cu₉** at 150(2) K without optimization. The first Brillouin zone was sampled with a grid spacing of 0.005 Å⁻¹ for wave functions and 0.05 Å⁻¹ for the density of states (DOS) on the basis of the Monkhorst–Pack special k-point scheme.[40]

Conflicts of interest

There are no conflicts to declare.

Acknowledgements

Notes and references

1 J. C. Love, L. A. Estroff, J. K. Kriebel, R. G. Nuzzo and G. M. Whitesides, *Chem. Rev.*, 2005, **105**, 1103–1169.

2 W. A. Lopes and H. M. Jaeger, *Nature*, 2001, **414**, 735–738.

3 Y. He, T. Ye, M. Su, C. Zhang, A. E. Ribbe, W. Jiang and C. Mao, *Nature*, 2008, **452**, 198–201.

4 J.-F. Ayme and J.-M. Lehn, *Adv. Inorg. Chem.*, 2018, **71**, 3–78.

5 M. Barboiu, A.-M. Stadler and J.-M. Lehn, *Angew. Chem., Int. Ed.*, 2016, **55**, 4130–4154.

6 Y. Kim, M. F. Mayer and S. C. Zimmerman, *Angew. Chem., Int. Ed.*, 2003, **42**, 1121–1126.

7 P. Teng, Z. Niu, F. She, M. Zhou, P. Sang, G. M. Gray, G. Verma, L. Wojtas, A. van der Vaart, S. Ma and J. Cai, *J. Am. Chem. Soc.*, 2018, **140**, 5661–5665.

8 A. Coskun, M. Banaszak, R. D. Astumian, J. F. Stoddart and B. A. Grzybowski, *Chem. Soc. Rev.*, 2012, **41**, 19–30.

9 L. S. Xie, L. Sun, R. Wan, S. S. Park, J. A. DeGayner, C. H. Hendon and M. Dincă, *J. Am. Chem. Soc.*, 2018, **140**, 7411–7414.

10 L. Sun, C. H. Hendon, S. S. Park, Y. Tulchinsky, R. Wan, F. Wang, A. Walsh and M. Dincă, *Chem. Sci.*, 2017, **8**, 4550–4557.

11 J. V. Barth, G. Costantini and K. Kern, *Nature*, 2005, **437**, 671–679.

12 Y.-K. Deng, H.-F. Su, J.-H. Xu, W.-G. Wang, M. Kurmoo, S.-C. Lin, Y.-Z. Tan, J. Jia, D. Sun and L.-S. Zheng, *J. Am. Chem. Soc.*, 2016, **138**, 1328–1334.

13 L.-Y. Guo, H.-F. Su, M. Kurmoo, C.-H. Tung, D. Sun and L.-S. Zheng, *J. Am. Chem. Soc.*, 2017, **139**, 14033–14036.

14 F. Yu, J. Li, Z.-H. Cao, M. Kurmoo and J.-L. Zuo, *Inorg. Chem.*, 2018, **57**, 3443–3450.

15 J. Janculev and B. Podolesov, *God. Zb., Filoz. Fak. Univ., Skopje, Prir.-Mat. Oddel*, 1958, **11**, 47–49.

16 S. Terashima, G. N. Newton, T. Shiga and H. Oshio, *Inorg. Chem. Front.*, 2015, **2**, 125–128.

17 Z.-L. Wu, C.-H. Wang, B. Zhao, J. Dong, F. Lu, W.-H. Wang, W.-C. Wang, G.-J. Wu, J.-Z. Cui and P. Cheng, *Angew. Chem., Int. Ed.*, 2016, **55**, 4938–4942.

18 M. B. Robin and P. Day, *Adv. Inorg. Chem. Radiochem.*, 1968, **10**, 247–422.

19 S. H. Vosko, L. Wilk and M. Nusair, *Can. J. Phys.*, 1980, **58**, 1200–1211.

20 T. Lu and F. Chen, *J. Comput. Chem.*, 2012, **33**, 580–592.

21 N. F. Chilton, R. P. Anderson, L. D. Turner, A. Soncini and K. S. Murray, *J. Comput. Chem.*, 2013, **34**, 1164–1175.

22 A. W. Sandvik, *Phys. Rev. B: Condens. Matter Mater. Phys.*, 1999, **59**, R14157–R14160.

23 A. F. Albuquerque, F. Alet, P. Corboz, P. Dayal, A. Feiguin, S. Fuchs, L. Gamper, E. Gull, S. Gürtler, A. Honecker, R. Igarashi, M. Körner, A. Kozhevnikov, A. Läuchli, S. R. Manmana, M. Matsumoto, I. P. McCulloch, F. Michel, R. M. Noack, G. Pawłowski, L. Pollet, T. Pruschke, U. Schollwöck, S. Todo, S. Trebst, M. Troyer, P. Werner and S. Wessel, *J. Magn. Magn. Mater.*, 2007, **310**, 1187–1193.

24 S. Forrest, *Science*, 1993, **261**, 872–878.

25 Mercury CSD 3.9 (Build RC1), CCDC, 2016.

26 G. A. Bain and J. F. Berry, *J. Chem. Educ.*, 2008, **85**, 532–536.

27 G. M. Sheldrick, *SADABS—Bruker AXS Area Detector Scaling and Absorption*, 2008.

28 G. M. Sheldrick, *Acta Crystallogr., Sect. A: Found. Adv.*, 2015, **A71**, 3–8.

29 G. M. Sheldrick, *Acta Crystallogr., Sect. C: Struct. Chem.*, 2015, **C71**, 3–8.

30 P. van der Sluis and A. L. Spek, *Acta Crystallogr., Sect. A: Found. Crystallogr.*, 1990, **46**, 194–201.

31 A. D. Becke, *Phys. Rev. A: At., Mol., Opt. Phys.*, 1988, **38**, 3098–3100.

32 C. T. Lee, W. T. Yang and R. G. Parr, *Phys. Rev. B: Condens. Matter Mater. Phys.*, 1988, **37**, 785–789.

33 A. D. Becke, *J. Chem. Phys.*, 1993, **98**, 5648–5652.

34 M. J. Frisch, G. W. Trucks, H. B. Schlegel, G. E. Scuseria, M. A. Robb, J. R. Cheeseman, G. Scalmani, V. Barone, B. Mennucci, G. A. Petersson, H. Nakatsuji, M. Caricato, X. Li, H. P. Hratchian, A. F. Izmaylov, J. Bloino, G. Zheng, J. L. Sonnenberg, M. Hada, M. Ehara, K. Toyota, R. Fukuda, J. Hasegawa, M. Ishida, T. Nakajima, Y. Honda, O. Kitao, H. Nakai, T. Vreven, J. A. Montgomery Jr, J. E. Peralta, F. Ogliaro, M. Bearpark, J. J. Heyd, E. Brothers, K. N. Kudin, V. N. Staroverov, R. Kobayashi, J. Normand, K. Raghavachari, A. Rendell, J. C. Burant, S. S. Iyengar, J. Tomasi, M. Cossi, N. Rega, J. M. Millam, M. Klene, J. E. Knox, J. B. Cross, V. Bakken, C. Adamo, J. Jaramillo, R. Gomperts, R. E. Stratmann, O. Yazyev, A. J. Austin, R. Cammi, C. Pomelli, J. W. Ochterski, R. L. Martin, K. Morokuma, V. G. Zakrzewski, G. A. Voth, P. Salvador, J. J. Dannenberg, S. Dapprich, A. D. Daniels, Ö. Farkas, J. B. Foresman, J. V. Ortiz, J. Cioslowski and D. J. Fox, *Gaussian 09, rev. B.01*, Gaussian, Inc., Wallingford CT, 2009.

35 G. B. Bacskay, *Chem. Phys.*, 1981, **61**, 385–404.

36 A. Schäfer, C. Huber and R. Ahlrichs, *J. Chem. Phys.*, 1994, **100**, 5829–5835.

37 J. P. Perdew, K. Burke and M. Ernzerhof, *Phys. Rev. Lett.*, 1996, **77**, 3865–3868.

38 S. J. Clark, M. D. Segall, C. J. Pickard, P. J. Hasnip, M. I. J. Probert, K. Refson and M. C. Payne, *Z. Kristallogr.*, 2005, **220**, 567–570.

39 Z. Fei, Y. Shi, L. Pu, F. Gao, Y. Liu, L. Sheng, B. G. Wang, R. Zhang and Y. D. Zheng, *Phys. Rev. B: Condens. Matter Mater. Phys.*, 2008, **78**, 201402.

40 H. J. Monkhorst and J. D. Pack, *Phys. Rev. B: Solid State*, 1976, **13**, 5188–5192.